Interaction of a droplet spray with a turbulent plane air jet impacting a wall

S Ikardouchene, S Delaby, Xavier Nicolas

S Ikardouchene, S Delaby, Xavier Nicolas. Interaction of a droplet spray with a turbulent plane air jet impacting a wall. Experiments in Fluids, 2023, 64, 10.1007/s00348-023-03585-z . hal-03999798

HAL Id: hal-03999798
https://hal.science/hal-03999798v1
Submitted on 21 Feb 2023

Experiments in Fluids manuscript No.
(will be inserted by the editor)

Interaction of a droplet spray with a turbulent plane air jet impacting a wall

Application to the confinement of atmospheres contaminated with particles by air curtain

Syphax Ikardouchene, Stéphane Delaby,
Xavier Nicolas

Received: date / Accepted: date

Abstract Experiments are carried out to study the interaction of a spray of spherical micronic oil droplets with a turbulent plane air jet impacting a wall. The context is the separation of a contaminated atmosphere with passive particles from a clean atmosphere by using a dynamical air curtain. A spinning disk is used to produce the spray of oil droplets close to the air jet. The diameter of the produced droplets varies between 0.3 and 7 μm. The jet and particulate Reynolds numbers and the jet and Kolmogorov Stokes numbers are respectively equal to $Re_j = 13500$, $0.2 \leq Re_p \leq 5$, $0.002 \leq St_j \leq 0.8$ and $0.03 \leq St_K \leq 15$. The ratio of the jet height to nozzle width is $H/e = 10$. The flow properties in the experiments are measured by particle image velocimetry and are in good agreement with large eddy simulation results. The droplet/particle passing rate (PPR) through the air jet is measured by an optical particle counter. The PPR decreases with the increase of the droplet diameter for the studied droplet size range. Whatever the droplet size is, the PPR increases with time due to the presence of two large vortices on each side of the air jet that bring the droplets back to the jet. The accuracy and repeatability of the measurements are verified. The present results can be used to validate Eulerian/Lagrangian numerical simulations on the interaction of micronic droplets with a turbulent air jet.

Keywords impinging turbulent jet · air curtain · plane jet · passive droplets · spinning disk · optical particle counter · particle passing rate

PACS 47.27.i · 47.55.dr · 47.55.D

X. Nicolas (orcidID: 0000-0001-7161-6169)
Univ Gustave Eiffel, Univ Paris Est Creteil, CNRS, UMR 8208, MSME, F-77454, Marne-la-Vallée, France
Tel.: +33-1-60957314
E-mail: xavier.nicolas@univ-eiffel.fr

S. Ikardouchene and S. Delaby
CSTB, 24 rue Joseph Fourier, 38400 Saint-Martin-d'Hères, France
E-mail: syphax.ikardouchene@cstb.fr, stephane.delaby@cstb.fr

Contents

1 Introduction

Turbulent plane air jets impacting a wall and air curtains are used in industry and housing for a wide range of applications. For instance, the wiping of liquid films by impinging plane jets is used in the jet stripping process to control the coating thicknesses in the paper and galvanizing industries [21,10]. Since air curtains are able to partially confine cold and hot ambiances, they are used for the housing air-conditioning, to reduce the thermal losses at the entrance of buildings or between two rooms [12,42,41] and in the vertical refrigerated display cabinets of food shops [30,9]. They can also be used as particulate barriers, to separate a clean atmosphere from a polluted one [31]. Thus plane air jets are used to reduce the spreading of fumes and gaseous pollutants in building and tunnel fires [16,13,11,24]. They are also used in manual workstations and fume cupboards of laboratories for the aerosol confinement [4]. Recently the effectiveness of personalized air curtains have been considered for reducing the exposure to airborne cough droplets, in the context of COVID-19 [34,40]. In our applications, air curtains are used around abrasive rotative machines to limit the outside propagation of the emitted particles [17].

The objective of the present work is threefold: (i) to present an original experiment designed to analyze the interaction of micronic droplets with a turbulent plane air jet separating two atmospheres, one contaminated by the injection of a spray of oil droplets, the other initially uncontaminated; (ii) to evaluate the efficiency of this air jet as a particle barrier by measuring the time evolution of the droplet or particle passing rate (PPR), globally and for each class of droplet size; (iii) to provide reference experimental results to validate Eulerian/Lagrangian numerical simulations on the interaction of micronic droplets with a turbulent air jet.

In the literature, the research works on jets of rectangular cross section are very numerous. The present review is limited to some main experimental works on plane jets in the fully-developed turbulent regime, for jet Reynolds numbers larger than around $Re_j = 5000$. The free jet space development presents four main regions in the direction of the mean flow along the jet axis: the potential core just after the nozzle, a transition zone, a fully-developed region in which the velocity profiles are self-similar and the terminal zone in which turbulence is dissipated and the mean velocity tends to zero (Rajaratnam (1976) [33]). The mean velocity decreases along the jet, while the turbulence intensity increases to reach values around $I = 20$ to 25% in the fully developed region (Gutmark and Wygnanski (1976) [15] and Namer and Otugen (1988) [29]).

The dynamics of a turbulent jet impinging normally onto a flat surface is analyzed experimentally by Gutmark et al. (1978) [14] in air and by Khayrullina et al. (2017) [19] in water. A recent review on this configuration and air curtains is proposed by Khayrullina et al. (2017, 2019) [19,20]. For impinging jets, the free jet development region after the nozzle is amputated from the terminal zone which is replaced by the impinging region close to the impact wall. The impinging region is composed by the deflection and stagnation zones of the jet, in front of the nozzle, and by the wall jet zones in which two secondary jets develop on each side of the main jet, parallel to the impact wall (Beltaos and Rajaratnam (1973) [8], Martin (1977) [25]). The mean and turbulent velocity profiles of impinging jets depend on the jet height to nozzle width ratio, H/e, the jet Reynolds number, $Re_j = e\overline{V}_{av,0}/\nu$, with $\overline{V}_{av,0}$ the average jet velocity at the nozzle outlet, and the turbulence intensity at the jet nozzle outlet, I_0. The influence of Re_j and H/e is analyzed in details by Maurel and Solliec (2001) [27] on the flow dynamics and by Tu and Wood (1996 [38]) on the pressure field on the impact wall. The stability of the jet and its flapping around the wall stagnation point are studied by Antonia et al. (1983) [2] and Senter (2006) [35]. Arthurs and Ziada (2011) [3] analyze the Fourier spectra of the velocity field along the jet to detect the frequencies associated to the Kelvin-Helmholtz instabilities and the jet flapping.

The research works on the particle confinement by plane jets generally provide global results on the confinement efficiency as a function of the air curtain parameters. Nino et al. (2011) [31] studied the confinement by air curtains of different thicknesses, subjected to an orthogonal jet of droplets. A spray of multi-dispersed water droplets of average diameter 6.27 μm is generated using an airbrush. The study was carried out for different Reynolds numbers of the air curtain (from $Re_j = 4500$ to 25500), different nozzle thicknesses ($e = 1$, 2 and 4 cm) and different distances between the air jet and the injection point of the droplet spray (from 10 cm to 2 m). The main result is that the air curtain limits the transfer of droplets for the large Reynolds numbers, $Re_j = 25500$ and 16500, for which a confinement efficiency higher than 95% is obtained whatever the configuration for $e = 1$ and 2 cm. On the other hand, for $e = 4$ cm, the droplets pass through the air curtain whatever the conditions. At a fixed Reynolds number, the air curtain being thicker, its speed is lower and this leads to a drop in performance of the air curtain, allowing the droplet passage. The experiments by Luo et al. (2013) [23] on smoke confinement also showed that the width of the air jet played an important role on the confinement. It is all the more effective as the air curtain is wide for a jet speed fixed at 10 m/s. Shih et al. (2011) [36] experimentally and numerically showed, with gaseous ethanol as pollutant, that the height H of the air jet also influences the confinement efficiency: it is higher the lower the height of the jet.

Previous research works that analyzed in depth the evolution of the passing rate of the particles along the jet, or as a function of the particle diameter, are quite rare in the literature. To our knowledge, only Maurel (2001) [26] in his PhD thesis experimentally compares the velocity profiles along the jet with the concentration profiles of a gaseous tracer injected at the nozzle level. Two seeding methods are used. In the first, a gaseous tracer is injected in the entire air jet at the level of the blowing nozzle. In the second method, only half of the jet is seeded. The goal is to quantify the mass transfer through the jet and locate the place where it mainly occurs, from the measurement of the tracer concentration along the jet. Three jet aspect ratios are tested: $H/e = 5$, 25 and 50, for $Re_j = 13500$. For a very confined jet ($H/e = 5$), the mass transfer appears only at the end of the potential cone and increases rapidly at the level of the impact zone. For the ratios $H/e = 25$ and 50, a progressive decrease in tracer concentrations (increase of mass transfer) is observed after the end of the potential cone. Moreover, the more H/e increases, the lower the concentration and the average velocity on the jet axis and the more the air curtain is permeable to the passage of pollutants. The experiments by Maurel and Solliec (2001) [27,26] are partially reproduced by Large Eddy Simulations (LES) by Beaubert and Viazzo (2002, 2003) [5–7] for $H/e = 10$ and $Re_j = 3000$, 7500 and 13500. Two numerical methods are used in [5] to determine the space and time evolution of the concentration of a passive tracer: a Lagrangian simulation of passive particles at $Re_j = 3000$ and the solution of a filtered concentration equation at $Re_j = 7500$. The concentration profiles along the jet axis from the LES [5] are in qualitative agreement with the experimental results [26]: they show an increase of the mass transfer through the jet along the jet axis, with a maximum located at the end of its developed zone (beginning of the impact zone) where the turbulence intensity is maximum.

The configuration of the present experiment is similar to that in Maurel and Solliec (2001) [27,26] and Beaubert and Viazzo (2002, 2003) [5,7]: it is a vertical plane air jet of aspect ratio $H/e = 10$, at $Re_j = 13500$, confined between two horizontal flat plates and impinging normally onto the bottom plate. The air jet is crossed by a spray of micronic spherical oil droplets produced by a spinning disk. In section 2, the air jet dynamics is studied from PIV measurements, without injecting droplets or particles. In section 3, the spinning disk used for the droplet injection is presented and its influence on the air jet is analyzed. A special care is taken in the characterization of the generated spray of oil droplets and in the analysis of the influence of the operating conditions. In section 4, the spray is injected close to the air jet and the passage rate of the oil droplets through the jet is analyzed from concentration measurements with an optical particle counter (OPC). Note that droplets are referred to interchangeably as droplets or particles throughout the article.

2 Study of the impacting plane air jet without particle

2.1 Description of the experimental facility and PIV metrology

In order to characterize impacting plane air jets, the experimental device of Fig. 1 (left) was designed. A vertical plane air jet is generated by a centrifugal fan that blows air through a divergent and convergent channel, then through a rectangular nozzle of section width $e = 3\ mm$ in x-direction, length $d_y = 117.6\ mm$ in vertical y-direction and depth $d_z = 200\ mm$ in z-direction. This nozzle was manufactured by 3D printing with a stereolithography method with layers of 100 microns to obtain a smooth surface. The nozzle aspect ratio $d_z/e = 66.7$ ensures that the flow is statistically two-dimensional and free from the side wall effects when taking measurements in the transverse mid-plane of the jet at $z = d_z/2$ [32]. The nozzle outlet is located in the middle and flush with the upper horizontal wall of a rectangular channel of height $H = 3\ cm$ in the vertical y-direction, depth $d_z = 200\ mm$ in z-direction and length $L_x = 60\ cm$ in the horizontal x-direction (30 cm on each side of the jet). The jet average velocity at nozzle outlet is $\overline{V}_{av,0} = 65\ m/s$ and the maximum average velocity is $V_0 = \overline{V}_0(x = 0) = 69.23\ m/s$. The jet Reynolds number $Re_j = \overline{V}_{av,0}\, e/\nu \approx 13500$ and the opening ratio $H/e = 10$ are fixed in all the study.

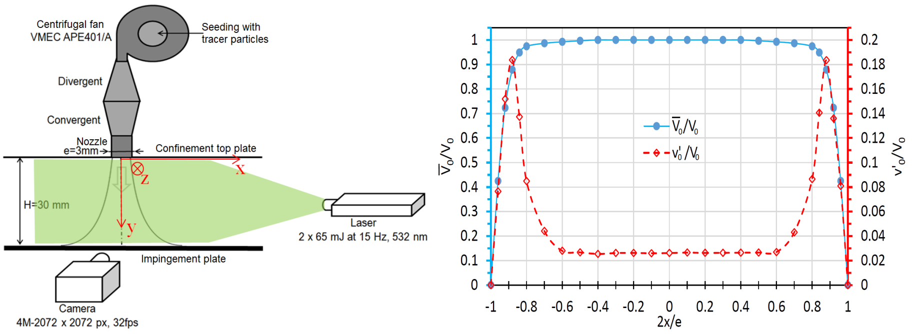

Fig. 1: Left: sketch of the experimental facility. Right: PIV horizontal profiles of the time averaged vertical velocity, $\overline{V}_0/V_0$, and turbulence intensity in the vertical direction, v'_0/V_0, at the nozzle exit.

The analysis of the velocity field is carried out by particle image velocimetry (PIV). A Dantec Dynamics DualPower Nd-Yag laser S65-15 (65 mJ, 15 Hz) and a fast camera FlowSense EO 4M-32 of 2072 × 2072 pixels^2 are used. To eliminate highlight phenomena, the confinement top plate and the impingement bottom plate were alternately coated with layers of matte black paint and rhodamine in order to force the laser reflections to be in the wavelength range 527-532 nm. Then a specific lens was used on the camera to precisely filter these wavelengths. Olive oil droplets are used as a tracer. They are injected directly at the fan level with a micron aerosol generator TSI 9306. Due to their volume fraction and their sub-micron diameter, these oil droplets are considered as passive particles in the air flow. A PIV system resolution of 2072×600 pixels^2 was used to visualize only the area of interest around the air jet and minimize computation time. The camera is placed at a distance of 50 cm from the laser vertical plane. The PIV processor ensures synchronization between the laser pulses and the camera shot. It saves the images in a buffer memory before transferring them to the storage disk on the acquisition PC. The buffer can store 366 pairs of images (732 independent samples) while operating at 15 Hz. The 366 pairs of images were considered to minimize errors when calculating the time averages and root mean square errors (RMSE) of the velocities. For the post-processing of the pairs of images, the "adaptive correlation" method was used with interrogation windows of dimensions 8×8 pixels^2 and with an overlap rate of 75% in both directions x and y. All the specifications of the laser and camera and the details of the followed experimental protocol are given in [17].

2.2 Analysis of the velocity field in the plane air jet without particle

In this section, the horizontal, U, and vertical, V, velocity components of the velocity vector, $\mathbf{V}$, measured in the transverse vertical median plane of the jet at $z = d_z/2$ are analyzed. The time averaged velocities are denoted with an over-line ($\overline{U}$, $\overline{V}$), the RMSE in lowercase with a prime (u', v') and the velocities at the nozzle outlet, at $y = 0$, with a zero subscript. The maximum time averaged velocity on the jet axis at nozzle exit is simply denoted by V_0. The horizontal profiles along the nozzle exit of the time averaged vertical velocity, $\overline{V}_0/V_0$, and turbulence intensity in the vertical direction, v'_0/V_0, are plotted on Fig. 1 (right). The time averaged velocity profile is symmetrical through the vertical median plane of the jet, $x = 0$. The turbulence intensity is approximately equal to 2.6% for $|2x/e| \leq 0.6$ and presents two peaks in the boundary layer whose maximum intensity is around 18%.

The PIV measurements are compared with the LES results by Ikardouchene et al. (2019, 2021) [17,18]. These LES are performed with the CFD code ANSYS/Fluent v18.2 using the WALE model for the sub-grid effects [1]. The numerical configuration imitates that of the experiments. The computational domain is a 3D rectangular box of size $L_x \times L_y(H) \times L_z = 243 \times 30 \times 18.84$ mm^3 in the horizontal, vertical and depth directions respectively. The vertical plane jet is injected into the domain by a nozzle of section $L_z \times e = 18.84 \times 3$ mm^2 located in the center of the upper horizontal wall. The time averaged velocity profile, $\overline{V}_0(x)$, measured at the outlet of the nozzle in the experiments (see Fig. 1 (right)) is interpolated and imposed as inlet boundary conditions in the LES. The average speed of this velocity profile is $\overline{V}_{av,0} = 65\, m/s$. Due to the physical property values chosen in the numerical simulations, the jet Reynolds number is equal to $Re_j = 13350$. Turbulent fluctuations are added to the average velocity profile of the inlet boundary condition by using a "spectral synthesizer" [1] with a turbulent intensity $I = 2\%$. No slip boundary conditions are imposed on the horizontal walls and periodic boundary conditions on the front and back faces in z-direction. The air jet impacts the lower wall and horizontally flows out through the left and right vertical openings, at $x = \pm L_x/2$, considered at atmospheric pressure. A non-uniform Cartesian mesh of size $N_x \times N_y \times N_z = 236 \times 150 \times 64$ cells ($y^+_{max} < 5.6$) is used. The time step is $\Delta t = 10^{-6}$ s. The time duration for the statistics is 0.1 s. More details about the geometry, mesh and numerical methods are given in [17,18].

Fig. 2 shows the streamtraces of the time averaged velocity field in the vertical median plane at $z = d_z/2$ in our PIV experiments and at $z = L_z/2$ in the LES. The high-velocity air jet generates a symmetrical time-averaged flow through the median plane $x = 0$, with two large recirculations on either side of the jet. The recirculation centers are located at $|x| = 6.3 \pm 0.3$ cm in PIV and at $|x| = 6.0 \pm 0.5$ cm in the LES.

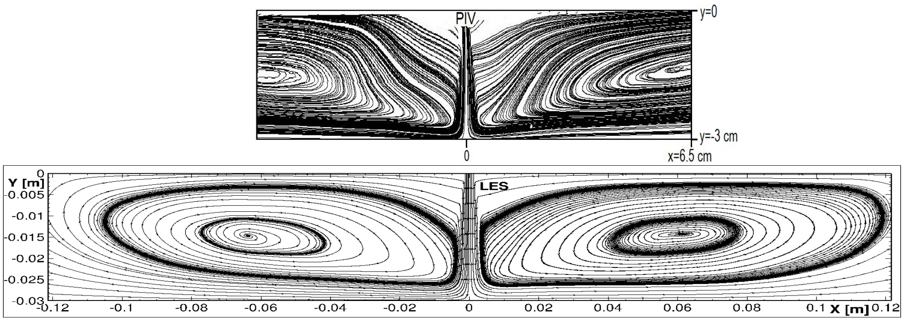

Fig. 2: Streamtraces of the time averaged velocity in the vertical median plane of the jet, at $z = d_z/2$ in the PIV experiments and at $z = L_z/2$ in the LES.

Figs. 3 to 5 show fields and profiles of the velocities measured by the present PIV. They are denoted "PIV" with turquoise stars in the captions of Figs. 4 and 5. They are compared, for the same configuration at $Re_j = 13500$ and $H/e = 10$, with the experimental results by Maurel (2001) [26] and Maurel and Solliec (2001) [27] (denoted "Exp Maurel" in the captions), the LES results by Beaubert (2002) [5] and Beaubert and Viazzo (2003) [7] (denoted "LES Beaubert") and our own LES results (denoted "LES (Wale)"). The different zones of the jet (potential core, developed zone, impact zone; see Fig. 4a) are recovered by the PIV measurements, as well as the turbulent fluctuation intensities. In particular, the maximum turbulent intensities are located close to the impact zone of the jet where they can reach 17 m/s for u' (see Figs. 3b and 4b) to 26 m/s for v' (see Fig. 4c). From the view point of the air curtain, these high turbulent intensity zones are the weak zones of the air curtain through which the particle transfer by the turbulent fluctuations is maximum [26,5]. Fig. 5 presents experimental and LES transverse profiles of the time averaged x- and y-velocity components, at different heights through the jet. All these profiles are in a good agreement. Thus all the present PIV measurements agree well with the literature results, both for the time averages and the RMSE of the velocities. Other validations, available in [17], were carried out by comparing other vertical and transverse profiles of the velocity components, pressure, Reynolds stresses and half width of the jet and Fourier spectra of time signals. All these results being also in good agreement with the reference results, it can then be considered that the test bench and the metrology used for the impinging air jet analysis are validated.

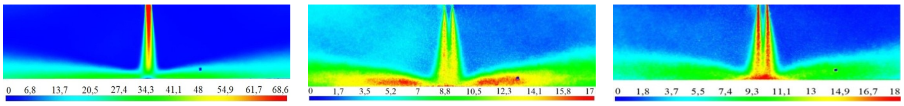

(a) Time average of the velocity magnitude, $||\overline{\mathbf{V}}||$ [m/s].
(b) Turbulent intensity of the horizontal velocity component, u'/V_0 [%].
(c) Turbulent intensity of the vertical velocity component, v'/V_0 [%].

Fig. 3: PIV fields of time average and RMSE of the velocity in the transverse vertical plane of the jet at $z = d_z/2$.

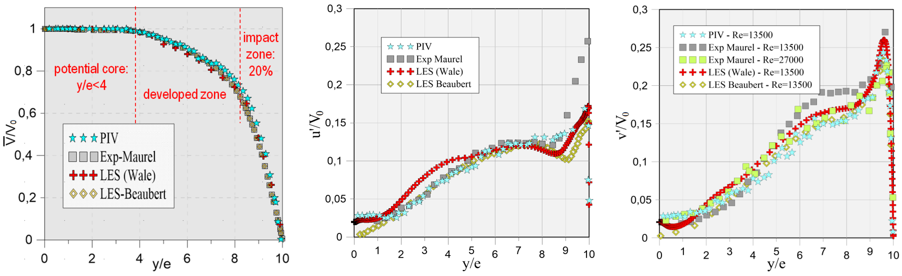

(a) Time average of the y-velocity component, $\overline{V}(y)$
(b) RMSE of the x-velocity component, $u'(y)$
(c) RMSE of the y-velocity component, $v'(y)$

Fig. 4: Profiles of the time averages and RMSE of the x- and y-velocity components along the jet y-axis, at $Re_j \approx 13500$ unless otherwise stated.

3 Study of the spinning disk and generated droplet spray

3.1 Influence of the operating conditions on the droplet spray

To study the interaction of particles with the impacting plane air jet, a spray of olive oil droplets is generated, but it is injected using the spinning disk method [39]. The aerosol generator TSI 9306 used for PIV is inactivated when the spinning disk is activated. The spinning disk principle is the fragmentation and dispersion of oil droplets under the centrifugal force of a rotating disk (Fig. 6). The advantage of this device is that it allows the injection of inertial particles without additional airflow which would be likely to modify the properties of the impacting air jet located nearby. In our experiment, the spinning disk

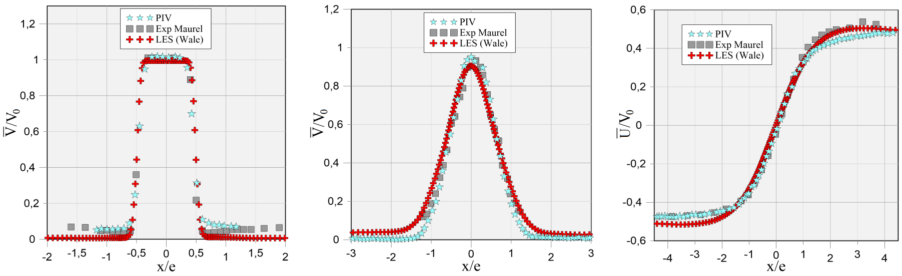

(a) $\overline{V}(x)$ at $y/e = 0.8$ (b) $\overline{V}(x)$ at $y/e = 5$ (c) $\overline{U}(x)$ at $y/e = 9.2$

Fig. 5: Profiles of the time averages of the x- and y-velocity components along the horizontal lines at $y/e = 0.8$, 5 or 9.2 and $z = d_z/2$, at $Re_j \approx 13500$.

is mounted on a rotative engine Dremel 8200 having a nominal maximum rotation speed $\omega = 30000$ rpm. An oil dash is deposited onto the center of the rotating disk (Fig. 6, right) under the action of the gravity force, from a 5-liter oil tank kept at a constant level. The tip of the liquid supply pipe is located nearly in contact with the disk center to create a capillary effect and ensure a continuous oil supply to the disk. The supply pipe contains a tap connected to a valve which allows the flow rate to be adjusted. Fairly low flow rates are imposed in order to obtain a stable and homogeneous generation of droplets. We have verified that this system makes it possible to impose the same oil flow rate from one test to another. We measured that the total angle of the spray ejection cone from the spinning disk is very small, around 3 deg. We can then consider that the droplets are ejected horizontally when the spinning disk is horizontal.

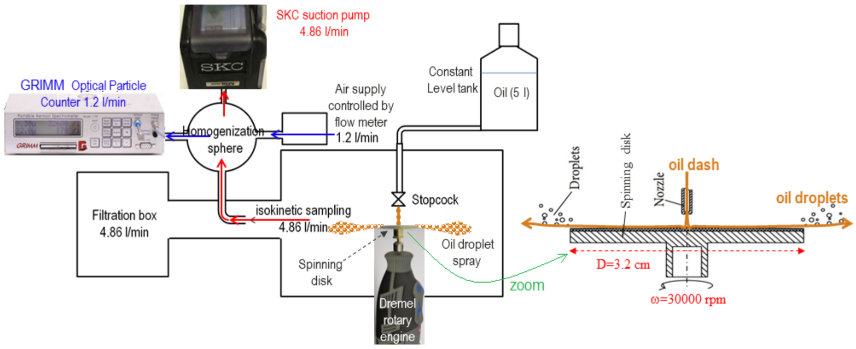

Fig. 6: Experimental test bench for the measurement by the Optical Particle Counter (OPC) of the concentration and size of the oil droplets emitted by the spinning disk and zoom on the spinning disk principle and characteristics.

To characterize the concentration and the size distribution of the oil droplets generated by the spinning disk, the test bench presented on Fig. 6 was used.

It consists of a closed volume in which the droplets are produced from the spinning disk, a suction pump to convey the droplets towards a homogenization sphere, and a GRIMM Optical Particle Counter 1.108 (OPC) which takes an isokinetic sample of the gas/droplet mixture. The OPC measures the size-resolved number concentration per liter of the droplets in the size range of 0.3 to 20 microns. In order to allow isokinetic sampling, the flow rate of air and droplets sucked by the GRIMM counter ($\approx 1.2\ l/min$) is exactly compensated.

First we analyzed the influence of several operating conditions acting on the measured concentration and size distribution of the droplets in the spray. For these tests, sprays of water droplets were considered to prevent possible fouling due to oil use. Some of the results obtained with water are presented in Fig. 7. We checked that same qualitative results are obtained with olive oil sprays. The studied parameters were the distance between the spinning disk and the tip of the collection tube of the OPC for $5 \leq d_{tube-disk} \leq 15\ cm$, the disk diameter for $3.2 \leq D_d \leq 6\ cm$, the spinning disk rotation speed for $15000 \leq \omega \leq 30000\ rpm$, the length of the droplet collection tube of the OPC for $5 \leq L_{tube} \leq 25\ cm$, and the injection flow rate of the liquid deposited on the spinning disk ($0.21 \leq \dot{m} \leq 5.9\ g/min$ for oil and $2.7 \leq \dot{m} \leq 9.7\ g/min$ for water). For all these initial tests, the droplet generation and the sampling were done over 5 minutes to have statistically converged and significant results. Each test was repeated between 3 and 5 times to determine the standard deviation of the measurements. And, before each measurement, the residual particle number in the ambient air was measured and subtracted from the results. In Figs. 7c, we observe that the residual number of droplets by air liter (green and blue curves) decreases with the increase of the droplet diameter, D_p, and is very low for $D_p \geq 1\ \mu m$ (smaller than 100 or even 10 droplets by liter).

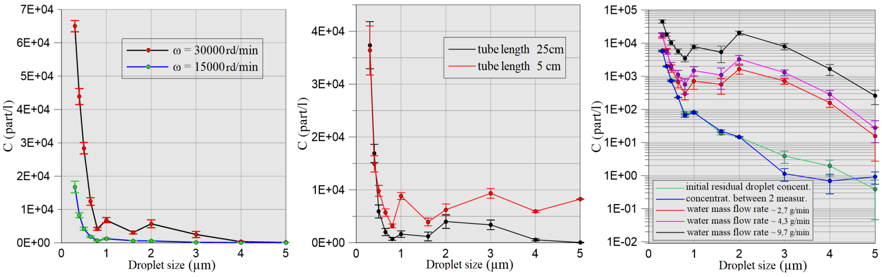

(a) Influence of the spinning disk rotation speed ω ($L_{tube}=25\ cm$)

(b) Influence of the length of the OPC collection tube L_{tube} ($\omega=30000\ rpm$)

(c) Influence of the water mass flow rate $\dot{m}$ ($L_{tube} = 25\ cm$, $\omega=30000\ rpm$)

Fig. 7: Influence of several parameters on the number concentration and size distribution of the droplets in the case of a water spray, for $D_d = 3.2\ cm$ ($T \approx 21.4°C$, $RH \approx 67\%$).

It has been checked that the distance $d_{tube-disk}$ between the spinning disk edge and the OPC collection tube tip, upstream the homogenization sphere, has a negligible influence on the measured droplet size distribution (not shown here). It appeared that the higher the disk diameter, D_d, the less reproducible was the spray generation because the more important was the standard deviation of the concentration measurements. Therefore, the smaller disk diameter $D_d = 3.2\ cm$ was retained for all the experiments. As shown on Fig. 7a, the higher the disk rotation speed ω, the larger the generated number of droplets is. Therefore, the maximum rotation speed $\omega = 30000\ rpm$ was retained for the following experiments with a spray of water droplets. It was also observed that the number of droplets decreases as a whole when their size increases from $D_p = 0.3$ to $4\ \mu m$ and the number of particles of size greater than $5\ \mu m$ is extremely small. However this was partly due to the droplet collection tube of the OPC whose length was equal to $L_{tube} = 25\ cm$ and internal diameter to $D_{tube} = 2\ mm$ in these preliminary experiments. Indeed Fig. 7b shows that the length of the droplet collection tube, for $L_{tube} = 5$ and $25\ cm$, has a great influence on the measured number concentration for the larger droplets of diameter $D_p \geq 3\ \mu m$. This is most likely due to the deposition of the bigger droplets on the wall of the long collection tube. For this reason, a short collection tube of length $L_{tube} = 5\ cm$ and $D_{tube} = 2\ mm$ was used in the final experiments with the oil droplet spray. However since the number of droplets of diameter $D_p \geq 6\ \mu m$ always remained very small, the abscissa of the presented graphs are limited to $D_p = 5\ \mu m$ even if some droplets of higher diameter were sometimes detected. The influence of the liquid mass flow rate $\dot{m}$ deposited on the spinning disk is presented on Fig. 7c. Is is observed that the measured number concentration is proportional to $\dot{m}$. For this reason, we always selected the smaller injection mass flow rate, particularly for the olive oil sprays ($\dot{m} = 0.21\ g/min$), to avoid fouling the experimental bench and the OPC.

3.2 Characterization of the spray of oil droplets

In order to limit the possible effects of evaporation of water droplets in 10 minute experiments, we decided to generate olive oil sprays. This choice was made in view of its preferred use in PIV to measure the speed of the fluid particles along their trajectory. We also observed a very stable generation of the oil spray by the spinning disk, i.e. a stable number concentration over time (see [17] for details). The parameters retained for all the experiments of this paper with an oil spray injection by the spinning disk are given in Tab. 1. Note that the rotation speed was slightly reduced at $\omega = 23000\ rpm$ for the experiments with an oil spray because small variations of ω were measured at the maximum nominal value of the rotative engine.

We first measured the granulometry of the generated oil droplets (Fig. 8). Five tests presented in Fig. 8a were done. As it can be viewed, a good repeatability of the measurements was verified. The number concentration of the droplets decreases as their diameter increases. The number of droplets with diameter $D_p \geq 6\ \mu m$ is very small, on the order of 10^3 droplets per air liter, with a relatively important dispersion. On the other hand, for $D_p = 5\ \mu m$, the

Table 1: Physical properties at atmospheric pressure and ambient temperature and parameters of the OPC and spinning disk for the experiments with an oil droplet spray.

Designation	Symbol	Value
ambient temperature	T	21 to 24°C
relative humidity	RH	55% to 70%
olive oil density	ρ_p	920 kg/m^3
olive oil surface tension	σ_p	0.032 N/m
air density	ρ	1.2 kg/m^3
air dynamic viscosity	μ	1.8 10^{-5} $kg/m.s$
air kinematic viscosity	ν	1.5 10^{-5} m^2/s
spinning disk radius	R_d	1.6 cm
spinning disk rotation speed	ω	23000 rpm
tangential speed of the spinning disk edge	$V_t = R_d\omega$	38.5 m/s
oil injection mass flow rate on the spinning disk	$\dot{m}$	0.2 g/min
suction flow rate of the OPC and isokinetic sampling	Q_s	1.2 l/min
length of the OPC tube for the droplet collection	L_{tube}	5 cm
diameter of the OPC tube for the droplet collection	D_{tube}	2 mm
distance between air jet axis and OPC collection point	$d_{tube-jet}$	20 cm
horizontal position of the spinning disk edge	x_{inj}	1 cm
vertical position of the spinning disk	y_{inj}	17 mm
duration of spray injection and OPC measurements	t_{inj}	5 to 10 min

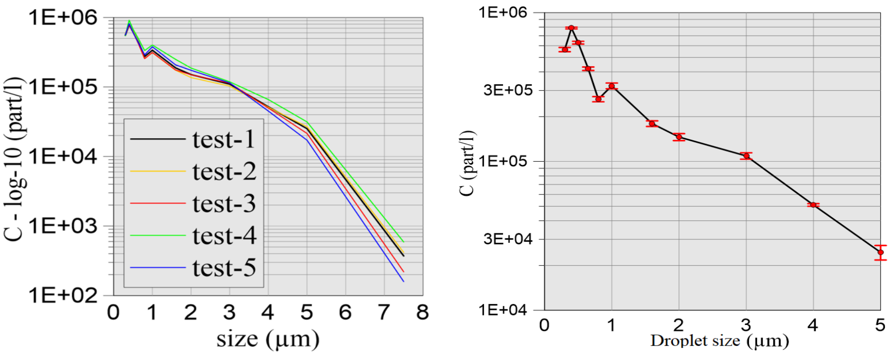

(a) Size distribution of the oil droplets in five tests.

(b) Mean size distribution of the oil droplets with standard deviation.

Fig. 8: Average number concentrations and size distributions of the generated droplets within the olive oil sprays.

number concentration, although still low, is not negligible. Therefore the mean concentration of the five tests is presented on Fig. 8b only for $0.3 \leq D_p \leq 5\ \mu m$, with very small error bars equal to the standard deviations. We can then conclude that the spinning disk generates oil droplets of diameters ranging from 0.3 to 5 μm with a number concentration that decreases almost monotonously with D_p. Fig. 8b will be able to be used as input data for numerical simulations which would attempt to reproduce the present experiments.

From the physical properties of air and olive oil of Tab. 1 and the data on the intensity of the turbulent fluctuations in Fig. 4, it is possible to evaluate a priori the dimensionless parameters characteristic of the behavior of the oil droplets in the present flow as a function of their size (see Tab. 2). The particulate Reynolds number, $Re_p = D_p|\mathbf{V} - \mathbf{V}_p|/\nu$, is estimated by considering that the velocity difference between the air flow and the droplets is at maximum on the order of the turbulent velocity fluctuations that is around $|\mathbf{V} - \mathbf{V}_p| \approx |\mathbf{V}'| \approx 10\ m/s$. The drag coefficient is approximated by $C_D(Re_p) = a_1 + \frac{a_2}{Re_p} + \frac{a_3}{Re_p^2}$ where the constants a_i $(i = 1, 2, 3)$ are given by Morsi and Alexander [28] as a function of Re_p. The particle relaxation time under the drag force effect is defined as $\tau_p = \frac{\rho_p D_p^2}{18\mu} \frac{24}{C_D Re_p}$ [1]. The Stokes numbers associated with the turbulent large scale or the jet scale are defined by $St_j = \tau_p/\tau_j$ and the one associated with the Kolmogorov scale by $St_K = \tau_p/\tau_K$. In these definitions, τ_j is the characteristic time for a droplet to cross the half width of the jet under turbulent fluctuations. It is evaluated by $\tau_j \approx e/(2|\mathbf{V}'|) \approx 1.5 \times 10^{-4}\ s$. It can also be considered as the characteristic time associated with the turbulent large scale (Kelvin-Helmholtz vortices). τ_K is the time associated with the turbulent small scale (Kolmogorov scale): it is defined by $\tau_K = (\frac{\nu}{\epsilon})^{1/2}$ with ϵ the turbulent dissipation. It can be approximated using the turbulent viscosity, ν_t, computed in the LES of the present air flow. Indeed, by considering the equilibrium between the production and dissipation of the turbulent kinetic energy and the LES Wale model [1], it can be shown [17] that $\epsilon \approx |\nu_t|^3/(C_W \triangle)^4$, where $C_W = 0.325$ is a constant of the Wale model, $\mathit{\Delta} = \sqrt[3]{\mathit{\Delta} x \mathit{\Delta} y \mathit{\Delta} z} \approx 6.10^{-5}\ m$ is the LES filter size linked to the used mesh, and $|\nu_t| \approx 3.75 \times 10^{-5}\ m^2/s$ is the average value of the turbulent viscosity in the air jet computed in the simulations described above. Therefore $\tau_K \approx (C_W \triangle)^2 \nu^{1/2}/|\nu_t|^{3/2} \approx 8.75 \times 10^{-6}\ s$. Finally the nature of the collision between two droplets is a function of the Weber number $We = \rho_p V_{p,rel}^2 D_p/\sigma_p$, where $V_{p,rel}$ is the relative velocity between two colliding droplets that can be approximated by $V_{p,rel} \approx |\mathbf{V}'| \approx 10\ m/s$ and σ_p is the droplet surface tension.

Thus, from the parameter values of Tab. 2, it appears that the air flow around the spherical droplets presents small inertial effects (non-Stokian behavior) whatever D_p since $0.2 \leq Re_p \leq 4.8$. The droplets of size $D_p < 4\ \mu m$ can be considered as passive scalars transported by the jet and the turbulent large scales since $St_j < 0.3$. On the other hand, from the view point of the turbulent small scales, the droplets of size $3 \leq D_p \leq 7\ \mu m$ present inertial effects because $3 < St_K < 14.4$. The droplets of size $D_p < 0.8\ \mu m$ still have a passive scalar behavior for the small turbulent scales because $St_K < 0.2$. Since the Weber number range is $2 < We \leq 20$ for $0.8 \leq D_p \leq 7\ \mu m$, coalescence of these droplets are possible. Furthermore, from [37], two droplets can only be submitted to bouncing or coalescence after collision, according to their impact parameter and the angle between their trajectories (reflexive and stretching separations, with satellite droplets, are not possible). Finally, due to the small size of the oil droplets in the present study, their break-up under the shear rate of the air flow is not possible. Indeed, an overestimation of

Table 2: Parameters associated with the oil droplets of the spray as a function of their diameter.

D_p $[\mu m]$	Re_p	C_D	τ_p $[s]$	St_j	St_K	We
0.3	0.21	116.5	2.58×10^{-7}	0.002	0.03	0.86
0.4	0.27	87.90	4.56×10^{-7}	0.003	0.05	1.15
0.5	0.34	70.87	7.07×10^{-7}	0.005	0.08	1.44
0.65	0.44	55.23	1.18×10^{-6}	0.008	0.14	1.87
0.8	0.55	45.49	1.76×10^{-6}	0.012	0.21	2.30
1	0.68	37.09	2.70×10^{-6}	0.018	0.32	2.88
1.6	1.10	18.22	8.79×10^{-6}	0.059	1.03	4.60
2	1.37	15.34	1.31×10^{-5}	0.087	1.52	5.75
3	2.05	11.09	2.71×10^{-5}	0.181	3.16	8.63
4	2.74	8.80	4.55×10^{-5}	0.304	5.31	11.5
5	3.42	7.37	6.80×10^{-5}	0.453	7.94	14.4
6	4.11	6.39	9.41×10^{-5}	0.627	11.0	17.3
7	4.79	5.68	1.23×10^{-4}	0.823	14.4	20.1

the shear capillary number $Ca = \frac{\mu|\dot{\gamma}|D_p}{2\sigma}$, where $|\dot{\gamma}|$ is the shear rate, provides $Ca < 5.10^{-5}$ for $D_p < 7$ μm. That is four magnitude orders below the critical value of the capillary number for the appearance of droplet breakup in the present configuration [22].

3.3 PIV measurement of the oil droplet speed in the spray

If it is considered that the oil droplets are ejected from the spinning disk at the tangential velocity of the edge of the spinning disk in the ambient air at rest, then the larger droplets of diameter $D_p = 5$ μm have a particulate Reynolds number $Re_p = D_p V_{p,i}/\nu = 13$ with an initial velocity $V_{p,i} = V_t = 38.5$ m/s (see Tab. 1). A Lagrangian model expressing the balance between the inertial and drag forces (by neglecting the gravity force) can be used to evaluate the distance $x_p(t)$ traveled by the droplet from the ejection time $t = 0$, by considering the oil droplets as solid spheres. It is simply obtained that $x_p(t) = d_{p,s}(1 - e^{-t/\tau_p})$, with $d_{p,s} = V_{p,i}\tau_p$ the droplet stopping distance and τ_p the particle relaxation time already defined above. For $D_p = 5$ μm and $Re_p = 13$, it is found that $C_D = 3.5$ [28], $\tau_p = 3.7 \times 10^{-5}$ s and the stopping distance of the larger droplets is only $d_{p,s} = 1.5$ mm. In reality, this theoretical computation of the stopping distance is oversimplified and not representative of the phenomena observed in the experiments because the ambient air is not at rest: an air flow is generated in the immediate vicinity of the spinning disk due to its high rotational speed and the ejection of the oil droplets. PIV measurements were therefore performed to determine the trajectory and velocity of the oil droplets ejected from the spinning disk.

The PIV measurements of the droplet speed were done without the presence of the plane air jet, in a radial vertical plane that passes through the spinning disk axis, as illustrated in Fig. 9a. It presents the velocity vectors in blue in a vertical plane located near the rotating disk. The velocity is maximum where the blue color is denser. Figs. 9b and 9c show the evolution of the average velocity and RMSE of the droplet velocity along the lines 1 and 2 (see the legends of Fig. 9). The droplets are ejected horizontally from the edge of the disk with an average speed close to $\overline{U}_{p,i} = 11\ m/s$ which decreases rapidly and loses more than 2/3 of its initial value in just 12 mm. Then the droplets are deflected downwards probably under the effect of the ambient airflow. Along the red line of Fig. 9a, the speed of the droplets continues to decrease until approximately $s = 28\ mm$ from the edge of the disk (see Fig. 9b). It then reaches a constant speed of the order of 0.8 m/s which corresponds to the average speed of the ambient air flow. Note in Fig. 9c the high amplitude of the RMSE of the droplet velocity, which is of the order of magnitude of the average speed, all along the measurement lines.

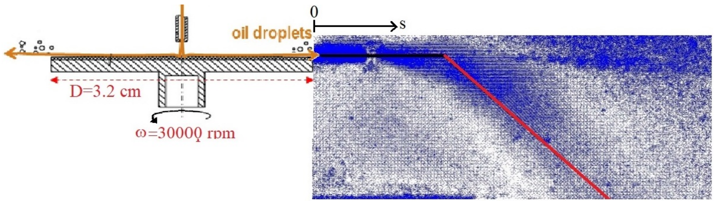

(a) Velocity vectors from PIV. Black line = “line 1” and red line = “line 2” in Figs. 9b, 9c.

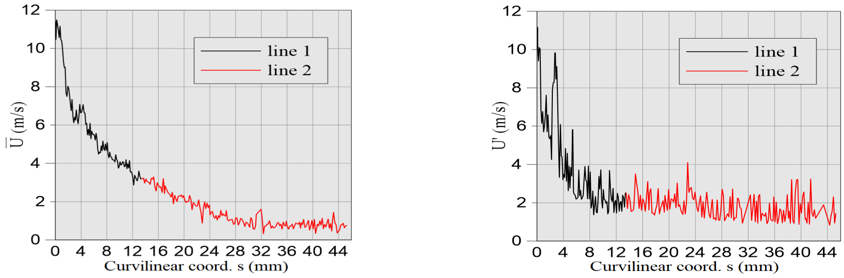

(b) Time averaged velocity of the oil droplets

(c) RMSE of the oil droplet velocity

Fig. 9: (a) Velocity vectors from the PIV (in blue) in a radial vertical plane near the spinning disk (without plane air jet). (b, c) Time average and RMSE of the horizontal velocity component of the oil droplets as a function of the curvilinear coordinate, s, along the two black and red lines of the top figure.

3.4 Influence of the spinning disk on the plane air jet development

It was checked by Ikardouchene et al. (2019, 2021) [17,18] that the presence of the spinning disk near the air jet does not disturb the latter. This verification was performed using the same PIV test bench as that described above by placing the spinning disk in a horizontal position, with its edge at $x = 10\,mm$ from the median vertical plane of the jet. The same PIV velocity profiles as in Fig. 4 were measured in three cases: in the absence of the rotating disk, in the presence of the disk stopped and in the presence of the disk rotating at $\omega = 30000\ rpm$. The average and RMSE velocity profiles of the three tests almost overlapping (see Fig. 5 in [18]), it was concluded that the disk has no impact on the development of the air jet when the distance between the two is $10\ mm$. That is why, in the present experiments, the spray injection distance $x_{inj} = 10\,mm$ is kept between the edge of the disk and the axis of the jet.

4 Study of the passing rate of the oil droplets through the impacting plane air jet

4.1 Test bench to measure the concentrations and passage rates of droplets

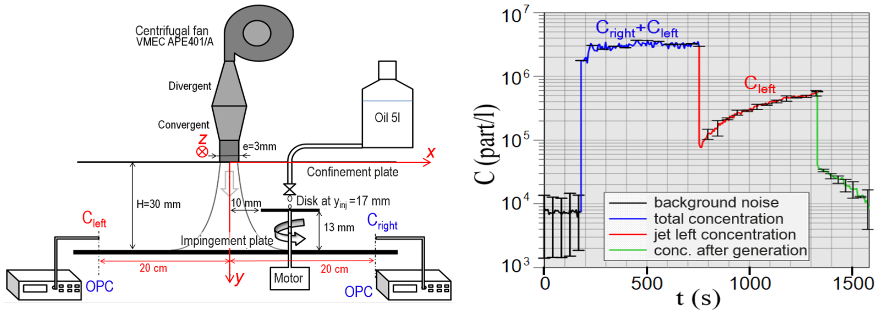

(a) Experimental facility for the jet/particle interaction study

(b) Time evolution of the total concentrations: $C_{right}(t) + C_{left}(t)$ and $C_{left}(t)$

Fig. 10: Sketch of the facility for the jet/droplet interaction study and concatenation of the time signals of the droplet total number concentrations.

The test bench to measure the passing rate of the oil droplets through the air jet is presented on Fig. 10a. All the operating conditions are given in Table 1. The spinning disk is located on the right of the jet which is therefore the zone contaminated by the oil droplets generated by the spinning disk. The left of the jet is the initially clean atmosphere. The droplet number concentrations and the size distributions are locally measured by the optical particle counter, OPC-GRIMM, on the two sides of the jet, at $x = \pm 20\ cm$. This position is well beyond the two large recirculations on each side of the jet since their length is around $14\ cm$ (see Fig. 8). We checked (not shown here) that, at $x = \pm 20\ cm$ from the jet, the measured concentrations are quasi homogeneous in all the channel section: they do not depend on y. The droplet number concentrations measured on the left of the jet are denoted C_{left} and C_{right} on the right of the jet, on the side of the rotating disk. The particle/droplet passing rate through the jet, denoted PPR, is defined as the ratio of the droplet number concentration in the initially clean zone of the channel to the number concentration of the whole injected droplets: $\mathrm{PPR}(t) = \frac{C_{left}(t)}{C_{left}(t)+C_{right}(t)}$. It is computed from the time signals of the number concentrations measured either for the total number of droplets (whatever their size, as in Fig. 10b for example) or for each class of droplet size, since the OPC can measure the diameter D_p of each droplet.

Four concentration signals recorded in the presence of the air jet are concatenated in Fig. 10b : (1, black) the concentration of the environment before the spray injection, in order to subtract it from the following measurements; (2, blue) the injected total concentration, $C_{left}+C_{right}$; (3, red) the concentration of droplets passing through the jet, C_{left}; (4, green) the left concentration after stopping the particle generation. C_{left} and C_{right} are measured every 6 seconds, during a ten minute spray injection. The repeatability of the measurements is illustrated by the standard deviation (error bars) resulting from three distinct tests. It is clear from this figure that the air jet plays its role of particulate barrier since C_{left} is much smaller than $C_{left} + C_{right}$. The average PPR resulting from these measurements (not shown here) approximately varies linearly from 4% to 17% in ten minutes.

The injection position of the rotating disk is at $y_{inj} = 17\ mm$ from the top confinement plate, at the level of the developed zone of the jet (see Figs. 4a and 10a). We checked that the vertical position of the spinning disk has nearly no influence on the measured concentrations and PPR due to the presence of the two large and turbulent recirculations on each side of the jet. Indeed, on the right of the channel, the evacuated droplets by the air jet, along the bottom plate towards the outlet, are taken back to the jet by the right vortex. Thus the two turbulent vortices tend to accumulate, mix and homogenize the droplets suspended in the air on either side of the jet. This accumulation over time is visible in Fig. 10b in which the left concentration $C_{left}(t)$ and the injected total concentration $(C_{right} + C_{left})(t)$ increase with time (it is not very clear for the total concentration due to the logarithmic scale).

4.2 Analysis of the passing rate of the oil droplets through the air jet

Fig. 11 presents the passing rate (PPR) of the droplets through the jet with respect to their diameter, for $0.3 \leq D_p \leq 4\ \mu m$. The PPR at $D_p = 5\ \mu m$ is not represented due to too small and dispersed concentration values and, as a consequence, a non representative and too large dispersion of the PPR values. In the two graphs of Fig. 11, the errors bars are equal to the standard deviation obtained from 3 trials. The time evolution of the PPR for each class of droplet diameter is plotted in Fig. 11a, each 6 second during ten minutes. The PPR increases with time for all the droplet sizes considered: the PPR is relatively small at the beginning of the spray injection (between 1.5% and 4%) but it reaches much larger values (between 8% and 18%) after ten minutes of injection. As already discussed above, the PPR increases with time due to the presence of the two large recirculations on either side of the air jet that “recycle” and accumulate the droplets [17]. The experimental curves can be

Table 3: Equations of the second order polynomials that interpolate PPR(t) of Fig. 12a over ten minutes for each class of droplet diameters.

D_p [μm]	Polynomial interpolation of PPR(t)
0.3	$3.8398 + 0.039243\ t - 2.4369 \times 10^{-5}\ t^2$
0.4	$2.9004 + 0.031008\ t - 1.4645 \times 10^{-5}\ t^2$
0.5	$2.7492 + 0.040402\ t - 2.2210 \times 10^{-5}\ t^2$
0.65	$2.1944 + 0.038934\ t - 2.2010 \times 10^{-5}\ t^2$
0.8	$1.8805 + 0.033983\ t - 1.8276 \times 10^{-5}\ t^2$
1	$1.8179 + 0.030221\ t - 1.5553 \times 10^{-5}\ t^2$
1.6	$1.4830 + 0.026126\ t - 1.4766 \times 10^{-5}\ t^2$
2	$1.1977 + 0.020217\ t - 1.2358 \times 10^{-5}\ t^2$
3	$1.1869 + 0.019110\ t - 1.4119 \times 10^{-5}\ t^2$
4	$1.4142 + 0.018161\ t - 1.0339 \times 10^{-5}\ t^2$

fitted by second order polynomials (dashed lines) whose equations are given in Tab. 3 with correlation coefficients in the range $0.96 \leq R^2 \leq 0.985$.

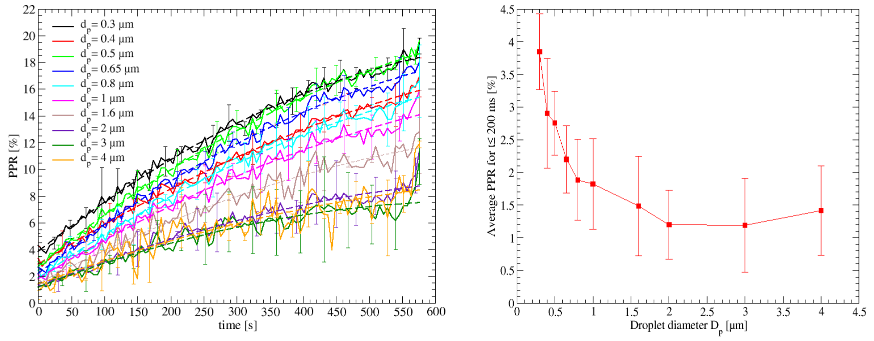

(a) PPR(t) for each class of droplet diameter with a second order polynomial interpolation (dashed lines).

(b) Time averaged PPR, interpolated from the polynomial interpolations of Fig. 11a for $t \leq 200$ ms.

Fig. 11: Droplet passing rate (PPR) through the jet with respect to the droplet diameter, D_p.

From these interpolation equations, it is possible to extract the average PPR over the first instants. This information can be important for numerical simulations because modeling and simulating such an experiment will be very CPU time consuming and the simulations will probably have to be limited to a few hundred milliseconds. Thus, Fig. 11b shows the time averaged PPR from $t = 0$ to $t = 200$ ms. The error bars on this figure are equal to the mean standard deviation of the PPR measured from the three tests during the first minute of the spray injection. The obtained PPR values are of course approximately equal to the constant term of the polynomials of Tab. 3. It appears in the two graphs of Fig. 11 that the PPR decreases on the whole when the droplet diameter increases. This behavior is hard to explain with the present experimental data. However, a thin film of oil is observed on the bottom impingement wall of the test bench, particularly on the right of the jet, after a ten minutes spray generation (but there is not oil film deposition on the top wall). Thus, one possible explanation could be that the larger droplets, whose Stokes numbers St_j and St_K are not negligible (see Tab 2), can cross the boundary layer and deposit on the bottom horizontal wall. This could therefore reduce their passing rate through the jet. Furthermore, this phenomenon could be amplified by the coalescence of the smaller oil droplets that could generate bigger ones. These phenomena are hard to detect with the measurements of the droplet size distribution by the OPC if the generated larger droplets immediately deposit on the wall. Furthermore, the number concentrations of the larger droplets in suspension in the air are too small to be significant. These conjectures could be verified by numerical simulations accounting for the droplet collision and coalescence and the deposition of the oil droplets on the wall.

The passing rate of the droplets through the jet, averaged over a ten minute experiment, was published in Fig. 7 of reference [18]. This average PPR decreases with the increase of the droplet diameter for $0.3 \leq D_p \leq 3\ \mu m$ but it increases with D_p for $D_p \geq 4\ \mu m$. This last result must not be considered because it is erroneous due to a faulty measurement of the number concentrations for $D_p \geq 4\ \mu m$.

5 Conclusion

This paper presents an original experiment designed to analyze the interaction of micronic droplets with a turbulent plane air jet separating two atmospheres. It allows to evaluate the efficiency of the air jet as a particle barrier by measuring the time evolution of the droplet passing rate (PPR), globally and for each class of droplet size. It also provides reference experimental results to validate Eulerian/Lagrangian numerical simulations on the interaction of micronic droplets with a turbulent air jet.

In the first part of the study, an experimental and numerical analysis of the air jet dynamics without injecting particles has been performed. The comparison of the present PIV and LES results with literature results has shown very good agreements, both for the time averages and the RMSE of the velocity components. The used Wale LES model is therefore appropriate to simulate a turbulent air jet impacting a wall.

In the second part, the interactions between this air jet and oil droplets (spherical particles) of different diameters has been investigated experimentally. The method of particle generation by a spinning disk has appeared to be a very interesting method because it is very stable over time, it does not perturb the jet and the generated spray of oil droplets is reproducible with a size distribution of the droplets between $0.3 \leq D_p \leq 5\ \mu m$. To allow this experiment to be reproduced by numerical simulations, particular care was taken to describe the test bench and the boundary and entry conditions. The droplet size distribution and injection speed are carefully determined.

It has been shown that the passing rate of the droplets through the jet increases with time due to the presence of two big recirculations on each side of the jet. It has also been observed that the passing rate decreases when the droplet diameter increases: at the first moments of the experiments, the PPR varies between 4% and 1.5% when D_p varies between 0.3 μm and 5 μm. This behavior could be due to the coalescence and the deposition on the impingement wall of the larger droplets. It was not possible to check this assertion with the used metrology. However it could probably be confirmed by numerical simulations accounting for the transport, the collision and the coalescence of the droplets (with a LES model for the continuous phase and a Lagrangian model for the discrete phase for instance).

Declarations

Ethical Approval

not applicable.

Competing interests

The authors declare that they have no competing interest or conflict of interest.

Authors'contributions

S.D. and X.N. supervised the project. S.I. and S.D. designed the experimental test bench and performed the experiments. X.N. designed and performed the numerical simulations. All authors contributed to the analysis and interpretation of the results. X.N. and S.I. wrote the manuscript. S.I. designed the figures.

Funding

SI and SD are grateful for the financial support granted by the Asbestos Research and Development Plan, launched in June 2015 by the French government, managed by the Department Housing, Urbanism, Landscapes, DHUP (Ministry of Territorial Cohesion). XN was supported by ANR and PIA via COMUE UPE and Isite FUTURE (contract no. ANR-16-IDEX-0003) as part of the CAPTEUR project.

Availability of data and materials

The data are available on request from the authors.

References

1. ANSYS: ANSYS Fluent Theory Guide, Release 18.2. Ansys Inc., Canonsburg (2017)
2. Antonia, R.A., Browne, L.W.B., Rajagopalan, S., Chambers, A.J.: On the organized motion of a turbulent plane jet. Journal of Fluid Mechanics **134**, 49–66 (1983). DOI https://doi.org/10.1017/s0022112083003213
3. Arthurs, D., Ziada, S.: The planar jet-plate oscillator. Journal of Fluids and Structures **27**, 105–120 (2011). DOI https://doi.org/10.1016/j.jfluidstructs.2010.10.002
4. Aubert, A., Solliec, C.: Push-pull air curtain performances for VOCs containment in an industrial process. Journal of Applied Fluid Mechanics **4** (2011). DOI https://doi.org/10.36884/jafm.4.01.11900
5. Beaubert, F.: Simulation des grandes échelles turbulentes d'un jet plan en impact. PhD thesis, Université de Nantes (2002). URL http://www.theses.fr/2002NANT2022

6. Beaubert, F., Viazzo, S.: Large Eddy Simulation of a plane impinging jet. C.R.A.S. Mécanique **330**, 803–810 (2002). DOI https://doi.org/10.1016/S1631-0721(02)01537-1
7. Beaubert, F., Viazzo, S.: Large Eddy Simulations of plane turbulent impinging jets at moderate reynolds numbers. International Journal of Heat and Fluid Flow pp. 512–519 (2003). DOI https://doi.org/10.1016/S0142-727X(03)00045-6
8. Beltaos, S., Rajaratnam, N.: Plane turbulent impinging jets. Journal of Hydraulic Research **11**(1), 29–59 (1973). DOI https://doi.org/10.1080/00221687309499789
9. Chen, Y.G.: Parametric evaluation of refrigerated air curtains for thermal insulation. International Journal of Thermal Sciences **48**(10), 1988 – 1996 (2009). DOI https://doi.org/10.1016/j.ijthermalsci.2009.03.003
10. Eßl, W., Pfeiler, C., Reiss, G., Ecker, W., Riener, C.K., Angeli, G.: LES-VOF simulation and POD analysis of the gas-jet wiping process in continuous galvanizing lines. Steel Research International **89**(2), 1700362 (2017). DOI https://doi.org/10.1002/srin.201700362
11. Gao, R., Li, A., Lei, W., Zhao, Y., Zhang, Y., Deng, B.: Study of a proposed tunnel evacuation passageway formed by opposite-double air curtain ventilation. Safety Science **50**, 1549–1557 (2012). DOI https://doi.org/10.1016/j.ssci.2012.03.007
12. Gonçalves, J.C., Costa, J.J., Figueiredo, A.R., Lopes, A.M.G.: CFD modelling of aerodynamic sealing by vertical and horizontal air curtains. Energy and Buildings **52**, 153–160 (2012). DOI http://dx.doi.org/10.1016/j.enbuild.2012.06.007
13. Gupta, S., Pavageau, M., Elicer-Cortés, J.C.: Cellular confinement of tunnel sections between two air curtains. Building and Environment **42**(9), 3352 – 3365 (2007). DOI https://doi.org/10.1016/j.buildenv.2006.08.026
14. Gutmark, E., Wolfshtein, M., Wygnanski, I.: The plane turbulent impinging jet. Journal of Fluid Mechanics **88**(4), 737–756 (1978). DOI https://doi.org/10.1017/S0022112078002360
15. Gutmark, E., Wygnanski, I.: The planar turbulent jet. Journal of Fluid Mechanics **73**(3), 465–495 (1976). DOI https://doi.org/10.1017/s0022112076001468
16. Guyonnaud, L., Solliec, C., Dufresne de Virel, M., Rey, C.: Design of air curtains used for area confinement in tunnels. Experiments in Fluids **28**(4), 377–384 (2000). DOI https://doi.org/10.1007/s003480050397
17. Ikardouchene, S.: Analyses expérimentale et numérique de l'interaction de particules avec un jet d'air plan impactant une surface. Application au confinement particulaire. PhD thesis, Univ. Paris Est (2019). URL https://www.theses.fr/2019PESC1046
18. Ikardouchene, S., Nicolas, X., Delaby, S., Ould-Rouiss, M.: Experiments and large eddy simulations on particle interaction with a turbulent air jet impacting a wall. In: M. Deville, C. Calvin, V. Couaillier, M. De La Llave Plata, J.L. Estivalèzes, T.H. Lê, S. Vincent (eds.) Turbulence and Interactions TI2018, *Notes on Numerical Fluid Mechanics and Multidisciplinary Design*, vol. 149, pp. 136–143. Springer International Publishing, Cham (2021). DOI https://doi.org/10.1007/978-3-030-65820-5_14
19. Khayrullina, A., van Hooff, T., Blocken, B., van Heijst, G.J.F.: PIV measurements of isothermal plane turbulent impinging jets at moderate Reynolds numbers. Experiments in Fluids **58**(4), 31 (2017). DOI https://doi.org/10.1007/s00348-017-2315-0
20. Khayrullina, A., van Hooff, T., Blocken, B., van Heijst, G.: Validation of steady RANS modelling of isothermal plane turbulent impinging jets at moderate Reynolds numbers. European Journal of Mechanics - B/Fluids **75**, 228–243 (2019). DOI https://doi.org/10.1016/j.euromechflu.2018.10.003
21. Lacanette, D., Gosset, A., Vincent, S., Buchlin, J.M., Arquis, E.: Macroscopic analysis of gas-jet wiping: Numerical simulation and experimental approach. Physics of Fluids **18**(4), 042103 (2006). DOI https://doi.org/10.1063/1.2186589
22. Lemenand, T., Dupont, P., Valle, D.D., Peerhossaini, H.: Comparative efficiency of shear, elongation and turbulent droplet breakup mechanisms: Review and application. Chemical Engineering Research and Design **91**(12), 2587–2600 (2013). DOI https://doi.org/10.1016/j.cherd.2013.03.017
23. Luo, N., Li, A., Gao, R., Tian, Z., Wei, Z., Mei, S., Feng, L., Ma, P.: An experiment and simulation of smoke confinement and exhaust efficiency utilizing a modified opposite double-jet air curtain. Safety Science **55**, 17 – 25 (2013). DOI https://doi.org/10.1016/j.ssci.2012.12.002. URL http://www.sciencedirect.com/science/article/pii/S0925753512002767

24. Luo, N., Li, A., Gao, R., Zhang, W., Tian, Z.: An experiment and simulation of smoke confinement utilizing an air curtain. Safety Science **59**, 10–18 (2013). DOI https://doi.org/10.1016/j.ssci.2013.04.009
25. Martin, H.: Heat and mass transfer between impinging gas jets and solid surfaces. Advances in Heat Transfer **13**, 1–60 (1977). DOI https://doi.org/10.1016/S0065-2717(08)70221-1
26. Maurel, S.: Etude expérimentale d'un jet plan en impact, analyse paramétrique et caractérisation des transferts de masse. PhD thesis, Ecole Polytechnique de l'université de Nantes (2001). URL https://www.theses.fr/2001NANT2037
27. Maurel, S., Solliec, C.: A turbulent plane jet impinging nearby and far from a flat plate. Experiments in Fluids **31**(6), 687–696 (2001). DOI https://doi.org/10.1007/s003480100327
28. Morsi, S., Alexander, A.: An investigation of particle trajectories in two-phase flow systems. Journal of Fluid mechanics **55**(2), 193–208 (1972). DOI https://doi.org/10.1017/S0022112072001806
29. Namer, I., Otugen, M.: Velocity measurements in a plane turbulent air jet at moderate reynolds numbers. Experiments in Fluids **6**(6), 387–399 (1988). DOI https://doi.org/10.1007/BF00196484
30. Navaz, H.K., Henderson, B.S., Faramarzi, R., Pourmovahed, A., Taugwalder, F.: Jet entrainment rate in air curtain of open refrigerated display cases. International Journal of Refrigeration **28**, 267–275 (2005). DOI https://doi.org/10.1016/j.ijrefrig.2004.08.002
31. Nino, E., Fasanella, R., Di Tommaso, R.M.: Submerged rectangular air jets as a particulate barrier. Building and Environment **46**(11), 2375–2386 (2011). DOI http://dx.doi.org/10.1016/j.buildenv.2011.05.020
32. Pope, S.B.: Turbulent Flows. Cambridge University Press (2000). DOI https://doi.org/10.1017/CBO9780511840531
33. Rajaratnam, N.: Turbulent jets, vol. 5. Elsevier (1976)
34. Sakharov, A.S., Zhukov, K.: Study of an air curtain in the context of individual protection from exposure to coronavirus (sars-cov-2) contained in cough-generated fluid particles. Physics **2**(3), 340–351 (2020). DOI 10.3390/physics2030018
35. Senter, J.: Analyse expérimentale et numérique des écoulements et des transferts de chaleur convectifs produits par un jet plan impactant une plaque plane mobile. PhD thesis, Université de Nantes (2006). URL http://www.theses.fr/2006NANT2099
36. Shih, Y.C., Yang, A.S., Lu, C.W.: Using air curtain to control pollutant spreading for emergency management in a cleanroom. Building and Environment **46**(5), 1104–1114 (2011). DOI http://dx.doi.org/10.1016/j.buildenv.2010.11.011
37. Sommerfeld, M., Pasternak, L.: Advances in modelling of binary droplet collision outcomes in sprays: A review of available knowledge. International Journal of Multiphase Flow **117**, 182–205 (2019). DOI https://doi.org/10.1016/j.ijmultiphaseflow.2019.05.001
38. Tu, C., Wood, D.: Wall pressure and shear stress measurements beneath an impinging jet. Experimental thermal and fluid science **13**(4), 364–373 (1996). DOI https://doi.org/10.1016/S0894-1777(96)00093-3
39. Walton, W.H., Prewett, W.C.: The production of sprays and mists of uniform drop size by means of spinning disc type sprayers. Proceedings of the Physical Society. Section B **62**(6), 341–350 (1949). DOI https://doi.org/10.1088/0370-1301/62/6/301
40. Xu, J., Guo, H., Zhang, Y., Lyu, X.: Effectiveness of personalized air curtain in reducing exposure to airborne cough droplets. Building and Environment **208**, 108586 (2022). DOI https://doi.org/10.1016/j.buildenv.2021.108586
41. Zhang, C., Yang, S., Shu, C., Wang, L.L., Stathopoulos, T.: Wind pressure coefficients for buildings with air curtains. Journal of Wind Engineering and Industrial Aerodynamics **205**, 104265 (2020). DOI https://doi.org/10.1016/j.jweia.2020.104265
42. Zhao, F.Y., Shen, G., Liu, K.J., Xu, Y., Liu, D., Wang, H.Q.: Room airborne pollutant separation by the use of air curtains in the large building enclosure: Infiltration efficiency and partial enclosure ventilation rate. Journal of Building Engineering **18**, 386–394 (2018). DOI https://doi.org/10.1016/j.jobe.2018.04.003